1 **Cortico-subcortical functional connectivity profiles of resting-state networks in**

2 **marmosets and humans**

3

4

5 **Abbreviated title:**

6 Cortico-subcortical networks in marmosets

7

8 **Authors and Affiliations:**

9 Yuki Hori[1], David J. Schaeffer[1], Atsushi Yoshida[2], Justine C. Cléry[1], Lauren K. Hayrynen[1],

10 Joseph S. Gati[1], Ravi S. Menon[1], Stefan Everling [1,3]

11 [1] Centre for Functional and Metabolic Mapping, Robarts Research Institute, The University of

12 Western Ontario, London, Ontario, Canada, N6A 5B7

13 [2] Laboratory of Sensorimotor Research, National Eye Institute, National Institutes of Health,

14 Bethesda, Maryland, USA, 20892

15 [3] Department of Physiology and Pharmacology, The University of Western Ontario, London,

16 Ontario, Canada, N6A 5C1

17

18 **Key words:** cortex, marmoset, resting-state functional MRI, subcortex

19

20 **Correspondence to:**

21 Stefan Everling, PhD

22 Centre for Functional and Metabolic Mapping, Robarts Research Institute, The University of

23 Western Ontario, London, Ontario, Canada, N6A 5B7

24 Tel: +1-519-931-5777 ext.24359

25 Email: severlin@uwo.ca

26

Author contribution: Y.H., D.J.S., A.Y. and S.E. designed research; Y.H., D.J.S., J.C.C., L.K.H., J.S.G. and S.E. performed research; Y.H., D.J.S. and A.Y. analyzed data; Y.H. wrote the paper; and Y.H., D.J.S., A.Y., J.C.C., L.K.H., J.S.G., R.S.M. and S.E. edited the paper.

Conflict of interest: The authors declare no conflict of interest.

Abstract

Understanding the similarity of cortico-subcortical networks topologies between humans and nonhuman primate species is critical to study the origin of network alternations underlying human neurological and neuropsychiatric diseases. The New World common marmoset (*Callithrix jacchus*) has become popular as a non-human primate model for human brain function. Most marmoset connectomic research, however, has exclusively focused on cortical areas, with connectivity to subcortical networks less extensively explored. In this study, we aimed to first isolate patterns of subcortical connectivity with cortical resting-state networks (RSNs) in awake marmosets using resting-state functional magnetic resonance imaging (RS-fMRI), then to compare these networks to those in humans using connectivity fingerprinting. While we could match several marmoset and human RSNs based on their functional fingerprints, we also found a few striking differences, for example strong functional connectivity of the default mode network with the superior colliculus in marmosets that was much weaker in humans. Together, these findings demonstrate that many of the core cortico-subcortical networks in humans are also present in marmosets, but that small, potentially functionally relevant differences exist.

Introduction

The New World common marmoset (*Callithrix jacchus*) has become popular as a model for human brain function (Okano et al., 2016). Owing to a developed frontal cortex (Okano and Mitra, 2015) and the feasibility of creating transgenic marmosets (Park et al., 2016; Sasaki et al., 2009; Tomioka et al., 2017a; Tomioka et al., 2017b), the marmoset has become a promising candidate for assessing neuropsychiatric disorders, especially those involving frontal impairments that are more difficult to study in rodent models (Okano and Mitra, 2015). In the past few years, marmoset brain connectomics, including corticocortical anatomical connections (Majka et al., 2020; Majka et al., 2016), functional networks/connections (Hori et al., 2020a; Hori et al., 2020b), and white matter pathways (Liu et al., 2020; Schaeffer et al., 2017), are becoming increasingly well-studied. In addition, similarities of these connections have been found between marmosets and humans (Liu et al., 2020; Schaeffer et al., 2019a; Schaeffer et al., 2019b; Solomon and Rosa, 2014).

Demonstrating homologies across species is a challenging endeavor due to both limitations in measuring networks using the same method across species, and in identifying analogous brain areas to compare across vastly different brain morphologies. Resting-state functional magnetic resonance imaging (RS-fMRI) allows for circumvention of some of these challenges by allowing for non-invasive identification of robust and reproducible resting-state networks across different species (Damoiseaux et al., 2006; Fox and Raichle, 2007; Smith et al., 2013; Sporns, 2013). With recent advances in MRI hardware, we are now able to measure the functional networks/connectivities in awake marmosets (Belcher et al., 2013; Cléry et al., 2020; Hori et al., 2020b; Schaeffer et al., 2019c). Particularly, the marmoset's small size is ideal for ultra-high field small-bore fMRI, affording high spatial resolution and signal-to-noise ratio (SNR) even in subcortical areas. Despite the ability to acquire MRI-based connectivity data in both marmosets and humans, the problem still stands of how to compare topologies amid major morphological differences. Connectivity fingerprinting have been offered as a method to circumvent this problem; this approach was originally proposed by Passingham and colleagues as a way to quantitatively evaluate the connections of a single cortical area with a

88   selected set of other areas (Passingham et al., 2002). More recently, Mars and colleagues

89   have suggested the feasibility of this approach as a tool for comparing various aspects of brain

90   organization across and within species (Balsters et al., 2020; Mars et al., 2018; Mars et al.,

91   2016; Schaeffer et al., 2020). Here, we employed this technique to compare cortico-subcortical

92   fingerprints of resting-state networks (RSNs) in marmosets and humans, allowing for

93   identification of inter-species similarities of cortico-subcortical connectivities.

94   We applied recent advances in hardware development for awake marmoset imaging,

95   including a custom-made multi-array coil, a gradient coil (Handler et al., 2020), and an

96   integrated head-fixation system (Schaeffer et al., 2019c) designed for small-bore ultra-high

97   field MRI (9.4 T). This system allows for nearly motion-less, high spatial resolution, and signal-

98   to-noise ratio (SNR) images. For human analyses, we used openly available datasets from the

99   Human Connectome Project (HCP) (Van Essen et al., 2013). We used a data-driven approach

100   via independent component analysis to identify RSNs in both marmosets and humans, then

101   specified the subcortical connections with each cortical RSN. The cortico-subcortical functional

102   fingerprints were created based on subcortical volumes of interests (VOIs), and were used to

103   identify putative homologous RSNs between marmosets and humans.

104

105   **Results**

106   *Cortico-subcortical RSNs in marmosets*

107   The overarching objective of this study was to identify the subcortical areas related to each

108   cortical RSN in marmosets, then to compare these cortico-subcortical connections between

109   marmosets and humans. To do so, we first identified cortical functional networks in the

110   marmosets (see Supplementary Fig. 1). After implementation of group ICA (Beckmann and

111   Smith, 2004) using awake RS-fMRI data in only cortical regions, 6 components were identified

112   as unstructured and/or physiological noise. The remaining 14 components demonstrated

113   meaningful RSNs (Fig. 1). These RSNs were thresholded at z = 2.3 for visual purposes.

114   Obtained RSNs were consistent with previously observed networks in marmosets (Belcher et

115   al., 2013; Ghahremani et al., 2016; Hori et al., 2020b) such as default mode network (DMN)

116   (Fig. 1A), attention network (ATN) (Fig. 1B), salience network (SAN) (Fig. 1C), left and right

117   primary visual networks (pVIS-Lt/Rt) (Figs. 1D, 1E), orbitofrontal network (ORN) (Fig. 1F), high-

118   order VISs (hVIS1-4: Fig. 1G-J), somatomotor networks ventral part (SMNv: Fig. 1K), dorsal

119   part (SMNd: Fig. 1L) and medial part (SMNm: Fig. 1M), and premotor network (PMN: Fig. 1N).

120   We calculated correlation coefficients between the time courses in each cortical RSN

121   and the time courses in each subcortical voxel. The functional connectivity maps (z-score

122   maps) in the subcortical areas were then averaged across scans. Averaged z-score values in

123   each subcortical area corresponding to each RSN are shown in Supplementary Fig 2, and

124   representative activation maps (z-score maps) are presented in Fig. 2. These z-score maps

125   were normalized to be maximum z-value equal to 1 and were thresholded at 0.2 for visual

126   purposes. The main subcortical area in the DMN (corresponding to Fig. 1A) was the

127   hippocampus (Fig. 2A), which is already known as a part of DMN in humans (Greicius et al.,

128   2004), macaques (Mantini et al., 2011; Vincent et al., 2007), and rats (Lu et al., 2012). The ATN

129   (corresponding to Fig. 1B) was strongly functionally connected with caudate and putamen (Fig.

130   2B). The primary subcortical area connected to the SAN (corresponding to Fig. 1C) was the

131   inferior colliculus (IC) (Fig. 2C). The primary VISs (corresponding to Fig. 1D and 1E) exhibited

132   strong functional connectivities with the lateral geniculate nucleus (LGN), superior colliculus

133   (SC), and ventral lateral (VL), ventral posterior (VP), and pulvinar thalamic nuclei (Fig. 2D).

134   These activations were found in both left and right visual networks. The main subcortical areas

135   in the ORN (corresponding to Fig. 1F) were the ventral striatum, caudate, putamen, and

136   anterior (ANT), laterodorsal (LD), mediodorsal (MD), ventral anterior (VA), and VL thalamic

137   nuclei (Fig. 2E). The main subcortical areas in the higher-order VIS were the SC and LGN for

138   hVIS3 and hVIS4 (Fig. 2F), while there was functional connectivity with the caudate and

139   putamen in these subcortical regions for hVIS1 and hVIS2. In the somatomotor networks, the

140   main subcortical components were the hippocampus and VP thalamic nucleus for the lateral

141   and medial networks (Fig. 2G). In the premotor network, the main subcortical component was

142   VL thalamic nucleus (Fig. 2H). To assign subcortical voxels to networks, the correlation

143   coefficients between the time courses in each cortical network and the time courses in each

144   subcortical voxel were calculated and Fisher's z-transformed. Then, the network with the

145   highest z-value among all networks was selected and assigned as the main network related to

146   the voxel (Fig. 3).

147

148   *Cortico-subcortical networks in humans*

149   For human RSNs, 10 components were identified as unstructured and/or physiological noise.

150   The remaining 10 components were identified as meaningful functional neural networks. These

151   RSNs were thresholded at z = 3.1 for visual purposes and were named based on the main

152   activation areas with reference to the recent paper, where each cortical partition is assigned to

153   one of the networks (Ji et al., 2019). As such, we identified the DMN (Supplementary Fig. 3A),

154   frontoparietal network (FPN) (Supplementary Fig. 3B), ATN (Supplementary Fig. 3C), two

155   SMNs (ventral: Supplementary Fig. 3D, dorsomedial: 3E), auditory network (AUD)

156   (Supplementary Fig. 3F), two VISs (primary: Supplementary Fig. 3G, high-order:

157   Supplementary Fig. 3H), language network (LAN) (Supplementary Fig. 3I) and cingulo-

158   opercular network (CON) (Supplementary Fig. 3J). Subcortical areas corresponding to each

159   RSN are shown in Supplementary Fig 4. The main subcortical area in the DMN (corresponding

160   to Supplementary Fig. 3A) was the hippocampus (Supplementary Fig. 4A). The FPN

161   (corresponding to Supplementary Fig. 3B) was connected with the caudate and putamen

162   (Supplementary Fig. 4B). The primary subcortical areas connected to the ATN (corresponding

163   to Supplementary Fig. 3C) were the amygdala, SC, and VP and pulvinar thalamic nuclei

164   (Supplementary Fig. 4C). In the SMNs (corresponding to Supplementary Fig. 3D and 3E), the

165   main subcortical components were the hippocampus and VP thalamic nucleus for both ventral

166   and lateral networks (Supplementary Fig. 4D and 4E). The AUD (corresponding to

167   Supplementary Fig. 3F) were functionally connected to all thalamic nuclei (Supplementary Fig.

168   4F). The primary VIS (corresponding to Supplementary Fig. 3G) exhibited strong functional

169   connectivity with the LGN, SC, and VP and pulvinar thalamic nuclei (Supplementary Fig. 4G),

170   and these activations were also found in the high-order VIS (Supplementary Fig. 3H and 4H).

171   The main subcortical areas in the LAN (corresponding to Supplementary Fig. 3I) were the

172   caudate nucleus and amygdala (Supplementary Fig. 4I). The main subcortical areas in the

173   CON (corresponding to Supplementary Fig. 3J) were the putamen and, ANT, MD, and LD

174   thalamic nuclei (Supplementary Fig. 4J). These subcortical connections in each network were

175   consistent with a previous study (Ji et al., 2019), where they showed caudate, putamen,

176   hippocampus, and amygdala were correlated with FPN, CON, DMN/SMN, and LAN,

177   respectively. The SC and LGN were correlated with primary VIS, which was also consistent

178   with our results. Generally, the subcortical connections except for thalamic nuclei in each

179   human network were similar to the corresponding marmoset networks. For both species, for

180   example, the DMN included hippocampus, and the VIS included LGN and SC. However,

181   thalamic connections in the VIS did not match between marmosets and humans. The VIS in

182   marmosets was strongly connected to the VL thalamic nucleus, while the VIS in humans was

183   mainly connected to the VP and pulvinar thalamic nuclei.

184

185   *Comparison of subcortical connectivity profiles*

186   Manhattan distance was used to quantitatively determine how well each subcortical

187   connectivity profile in marmoset RSNs matched the connectivity profile of corresponding

188   human RSNs. Connectivity fingerprints were created for marmosets and humans by

189   determining the mean z-values in seven target regions placed in caudate, putamen,

190   hippocampus, amygdala, SC, IC, and LGN. We did not include the other thalamic VOIs in the

191   fingerprint analysis as these regions are prone to residual global artifacts (Ji et al., 2019).

192   Permutation tests were performed to evaluate statistically significant matches between human

193   and marmoset fingerprints. For each of the ten human RSNs, we tested the hypothesis that the

194   difference between the fingerprints in humans and the target fingerprint in marmosets was

195   smaller than expected by chance. As such, we calculated the Manhattan distance with 10,000

196   different permutations of the target VOIs in marmosets, following normalization of each

197   fingerprint to a range of 0 (weakest functional connection with any of the target regions) and 1

198   (strongest functional connection with any of the target regions). A value less than 5 percentile

199   of the histogram of Manhattan distance was considered to be significantly similar fingerprints

200   across species.

201   The results revealed a number of significant matches between human and marmoset

202   RSNs based on their fingerprints (Fig. 4). The human DMN significantly matched with the

203 marmoset DMN with the strong hippocampus connections (p < 0.05), while the marmoset DMN

204 also exhibited strong FC with the SC (Fig. 5). The FPN in humans had similar subcortical

205 patterns to the ATN, ORN, and VIS1 in marmosets with caudate and putamen connections (p <

206 0.05; Fig. 6), but the fingerprint of the human ATN did not match with the fingerprint of the

207 marmoset frontoparietal network that we previously labeled ATN in marmosets (Hori et al.,

208 2020b). Instead, in addition to a match with the human FPN, the fingerprint of the marmoset

209 ATN network also matched with the fingerprint of the human LAN (p<0.05; Fig. 7). The primary

210 VIS in humans matched the marmoset primary VIS, high-order VIS3, and VIS4 with strong

211 connections to the SC and LGN (p < 0.05; Fig. 8). The secondary VIS in humans also matched

212 the marmoset high-order VIS (p < 0.05; Fig. 9). The CON in humans matched the marmoset

213 ORN and VIS1 (p < 0.05; Fig. 10).

214

215 **Discussion**

216 In the present study, we identified the cortico-subcortical functional connections of RSNs in

217 marmosets, then matched these networks with similar human networks based on the

218 fingerprints of their cortico-subcortical functional connectivity profiles. We found that the

219 cortico-subcortical fingerprints of several RSNs matched between marmosets and humans,

220 suggesting a similar functional cortico-subcortical organization of these networks in these two

221 species.

222   The DMN includes the hippocampus not only in humans (Greicius et al., 2004), but

223 also in macaques (Mantini et al., 2011; Vincent et al., 2007), and rats (Lu et al., 2012). Our

224 results showed that the marmoset DMN includes the hippocampus as well, indicating that it

225 may be a conserved feature across species. Note, however, that the cortical DMN in

226 marmosets was also functionally connected to the SC, which is not the case for the human

227 DMN. In addition to this difference in subcortical connectivity, the marmoset DMN includes a

228 fairly large parietal region that includes areas LIP, VIP, and MIP. Microstimulation in this region

229 around the shallow intraparietal sulcus evokes contralateral saccades (Ghahremani et al.,

230 2019) and single neurons in this region are active for saccadic eye movements (Ma et al.,

231 2020). On the other hand, the parietal region of the human DMN does not include the parietal

232   eye fields defined by multi-modal MRI techniques (Glasser et al., 2016). This discrepancy

233   might produce the difference of the connections with the SC between the species. It also

234   suggests that the marmoset DMN may not have sub serve all of the same functions as the

235   human DMN.

236   The marmoset ATN consisted of ventral frontal areas (8aV, 45), which are associated

237   with small saccadic eye movements (Selvanayagam et al., 2019). This network was mainly

238   connected to the caudate and putamen, and this subcortical activation pattern was consistent

239   with the human FPN, which includes the FEF and intraparietal areas that are involved in

240   saccade generation (Luna et al., 1998) and attention (Corbetta et al., 1998). Previous human

241   (Raemaekers et al., 2006; Raemaekers et al., 2002) and macaque studies (Hikosaka and

242   Wurtz, 1989; Phillips and Everling, 2012) have shown activations in the striatum (both caudate

243   and putamen) during saccade tasks. The parietal component of the marmoset ATN, however,

244   lies anterior to area LIP which is activated by saccadic eye movements (Schaeffer et al.,

245   2019d) and where saccades can be evoked by electrical microstimulation in marmosets

246   (Ghahremani et al., 2019), arguing perhaps against a pure role of this network in saccadic eye

247   movements. In fact, we found that the human language network (LAN) also matched the

248   marmoset ATN in terms of its cortico-subcortical connectivity fingerprint. In both species, the

249   networks showed strong functional connectivity with the caudate. In addition, there are also

250   clear similarities in the cortical regions between the marmoset ATN and the human LAN.

251   Broca's area (area 44, 45) is a prominent part of the human LAN and the marmoset ATN

252   network also includes area 45. Single neurons in marmoset area 45 and 8aV respond to

253   marmoset vocalizations and many are active for vocalizations (Miller et al., 2015), supporting a

254   role of this area in vocalization. The finding that the cortico-subcortical fingerprint of the ATN

255   matched with both the human FPN and the LAN may suggest that this core frontoparietal

256   network is the evolutionary precursor to these networks. Although we have labeled this network

257   as ATN here to be consistent with a previous paper (Hori et al., 2020b), a better label would

258   probably be just FPN for this network, consistent with an older report from our lab that used

259   ICA to identify RSNs in anesthetized marmosets (Ghahremani et al., 2016).

260   The subcortical pattern in the human FPN also showed a match to the marmoset

261   hVIS1. The main cortical activations in hVIS1 were along with the ventral visual stream

262   including TE3, V4T, and FST (Hung et al., 2015a; Schaeffer et al., 2019d). This is consistent

263   with human and macaque studies showing that the FPN includes a part of ventral visual stream

264   (Hutchison et al., 2012; Ji et al., 2019; Thomas Yeo et al., 2011). In addition, both human and

265   macaque FEF are functionally connected to these regions (Hutchison et al., 2012). As such,

266   the hVIS1 in marmosets seems to correspond to the temporal regions in the human FPN.

267   Interestingly, the subcortical pattern in the hVIS1 also showed a match to the human CON as

268   well as FPN. These two functional networks display increased activity during the performance

269   of complex cognitive tasks (Dosenbach et al., 2006; Sheffield et al., 2015; Wallis et al., 2015),

270   and both are associated with top-down control associated with executive functioning

271   (Dosenbach et al., 2007). Taken together with our findings, the marmoset hVIS1 might be

272   related to both FPN and CON through the putamen and caudate and play an important role in

273   top-down cognitive processing.

274   The cortical visual networks in marmosets were strongly connected to the SC, LGN,

275   VP, and PUL. These regions are known to be associated with the visual system (Hung et al.,

276   2015a; Hung et al., 2015b), and are structurally connected to visual-related cortices (Kaas and

277   Lyon, 2007; Solomon and Rosa, 2014; Zeater et al., 2019). We found that these subcortical

278   activation patterns in marmoset corresponded well to those in humans, suggesting that the

279   visual systems have a similar cortico-subcortical organization in both species. Previous

280   anatomical studies and electrophysiological recordings in marmosets have also shown that this

281   species' cortical visual hierarchy closely resembles that of other primates, including humans

282   (McDonald et al., 2014; Mitchell and Leopold, 2015; Yu and Rosa, 2010).

283

284   Conclusion

285   We have shown here that many of the marmoset RNSs can be matched to human RSNs

286   based on their cortico-subcortical fingerprint. While this suggests a similar cortico-subcortical

287   network organization in marmosets and humans, our results also show that there are

288 differences in the connectivity profiles that likely have consequences on the actual functions of

289 these RSNs. Electrophysiological and task-based fMRI studies in marmosets will be necessary

290 to further investigate functional similarities and differences in RSN organization between the

291 two species.

292

293 **Methods**

294 *Animal preparation*

295 All surgical and experimental procedures were in accordance with the Canadian Council of

296 Animal Care policy and a protocol approved by the Animal Care Committee of the University of

297 Western Ontario Council on Animal Care. All animal experiments complied with the Animal

298 Research: Reporting *In Vivo* Experiments (ARRIVE) guidelines. Four male common

299 marmosets weighting 390 g (3 years old), 245 g (1.5 years old), 330g (1.5 years old), and 360g

300 (1.5 years old), and one female marmoset weighting 306 g (1.3 years old) were used in *in-vivo*

301 and *ex-vivo* study, respectively.

302   Four marmosets for *in-vivo* experiments underwent surgery to implant a head

303 chamber to fix the head during MRI acquisition as described in previous reports (Johnston et

304 al., 2018; Schaeffer et al., 2019c). Briefly, the marmoset was placed in a stereotactic frame

305 (Narishige Model SR-6C-HT), and several coats of adhesive resin (All-bond Universal Bisco,

306 Schaumburg, Illinois, USA) were applied using a microbrush, air dried, and cured with an

307 ultraviolet dental curing light. Then, a dental cement (C & B Cement, Bisco, Schaumburg,

308 Illinois, USA) was applied to the skull and to the bottom of the chamber, which was then

309 lowered onto the skull via a stereotactic manipulator to ensure correct location and orientation.

310 The chamber was 3D printed at 0.25 mm resolution using stereolithography and a clear

311 photopolymer resin (Clear-Resin V4; Form 2, Formlabs, Somerville, Massachusetts, USA). The

312 marmosets were first acclimatized to the animal holder, head fixation system, and a mock MRI

313 environment prior to the first imaging session (Silva et al., 2011). Each marmoset was trained

314 over the course of three weeks. During the first week, marmosets entered the tube and were

315 constrained using only the neck and tail plates for increasingly long periods of time (up to 30

316   minutes). During the second week, the restraint tube was inserted into a mock MRI tube (a 12

317   cm inner diameter tube) to simulate the scanner environment; MRI sounds were played at

318   increasingly loud volumes (up to 80 dB) for increasingly long durations, up to 60 minutes

319   sessions. In week 3, marmosets were head-fixed via the fixation pins, inserted into the mock

320   MRI tube and exposed to the MRI sounds. Within each session, the animals are presented with

321   reward items (pudding or marshmallow fluff) for remaining still (calmly facing forward, with

322   minimal movement of limbs). Throughout the training sessions, the behavioral rating scale

323   described by Silva et al. (2011) was used to assess the animals' tolerance to the

324   acclimatization procedure by the end of week 3, all three marmosets scored 1 or 2 on this

325   assessment scale (Silva et al., 2011), showing calm and quiet behavior, with little signs of

326   agitation.

327   To create volumes of interests (VOIs) in subcortical area, we acquired *ex-vivo* MRI as

328   it allowed for longer scanning time at a much higher resolution (0.1 mm isotropic). To prepare

329   for *ex-vivo* MRI, one marmoset was euthanized through transcardial perfusion and its brain

330   was extracted at the end of the procedure. Anesthesia was initially induced with 30 mg/kg of

331   ketamine and maintained with 4% isoflurane in 1.5-2% oxygen. The animal was then

332   transcardially perfused with 0.9% sodium chloride solution, followed by 10% formaldehyde

333   buffered solution (formalin). The brain was then extracted and stored in 10% buffered formalin

334   for over a week.

335

336   *Image acquisition*

337   For the *in-vivo* experiment, each animal was fixed to the animal holder using a neck plate and

338   a tail plate. The animal was then head-fixed using fixation pins in the MRI room to minimize the

339   time in which the awake animal was head fixed (Schaeffer et al., 2019c). Once fixed, a

340   lubricating gel (MUKO SM321N, Canadian Custom Packaging Company, Toronto, Ontario,

341   Canada) was squeezed into the chamber and applied to the brow ridge to reduce magnetic

342   susceptibility.

343   Data were acquired using a 9.4 T 31 cm horizontal bore magnet (Varian/Agilent,

344   Yarnton, UK) and Bruker BioSpec Avance III HD console with the software package

345   Paravision-6 (Bruker BioSpin Corp, Billerica, MA), a custom-built high-performance 15-cm-

346   diameter gradient coil with 400-mT/m maximum gradient strength (Handler et al., 2020), and

347   the 5-channel receive coil (Schaeffer et al., 2019c). Radiofrequency transmission was

348   accomplished with a quadrature birdcage coil (12-cm inner diameter) built in-house. All imaging

349   was performed at the Centre for Functional and Metabolic Mapping at the University of

350   Western Ontario.

351   Functional images were acquired with 6-22 functional runs (at 400 or 600 volumes each) for

352   each animal in the awake condition, using gradient-echo based single-shot echo-planar

353   imaging sequence with the following parameters: TR = 1500 ms, TE = 15 ms, flip angle = 40°,

354   field of view (FOV) = 64 × 64 mm, matrix size 128 × 128, voxel size 0.5 mm isotropic, slices =

355   42, bandwidth = 500 kHz, generalized autocalibrating parallel acquisition (GRAPPA)

356   acceleration factor (anterior-posterior) = 2. Total scan time for all functional imaging was ~14h.

357   A T2-wighted image (T2w) was also acquired for each animal using rapid imaging with

358   refocused echoes (RARE) sequences with the following parameters: TR = 5500 ms, TE = 53

359   ms, FOV = 51.2 × 51.2 mm, matrix size = 384 × 384, voxel size = 0.133 × 0.133 × 0.5 mm,

360   slice 42, bandwidth = 50 kHz, GRAPPA acceleration factor (anterior-posterior) = 2.

361   For *ex-vivo* imaging, a formalin-fixed marmoset brain was submerged in lubricant

362   (Christo-lube; Lubrication technology Inc., Franklin Furnace, OH) to avoid magnetic

363   susceptibility-related distortion artifacts, and three-dimensional multi-echo spin-echo images

364   were acquired as following parameters: TR = 200 ms, TE = 3. 5, 8.5, 13.5, 18.5, 23.5 ms,

365   FOV = 33 × 28.8 × 36 mm, matrix size = 330 × 288 × 360, voxel size = 0.1 mm isotropic

366   resolution, average=4. The average image across different TE images was calculated to

367   increase the signal-to-noise ratio (SNR) and it was used to create the subcortical volume-of-

368   interests (VOIs).

369

370   *Marmoset image preprocessing*

371   Data was preprocessed using FSL software (Smith et al., 2004). Raw MRI images were first

372   converted to Neuro Informatics Technology Initiative (NIfTI) format (Li et al., 2016) and

373   reoriented from sphinx position. Brain masks for *in-vivo* images were created using FSL tools

374   and the National Institutes of Health (NIH) T2w brain template (Liu et al., 2018) For each

375   animal, the brain-skull boundary was first roughly identified from individual T2w using the brain

376   extraction tool (BET) with the following options; radius of 25-40 and fractional intensity

377   threshold of 0.3 (Smith, 2002). Then, the NIH T2w brain template was linearly and non-linearly

378   registered to the individual brain image using FMRIB's linear registration tool (FLIRT) and

379   FMRIB's nonlinear registration tool (FNIRT) to more accurately create the brain mask. After

380   that, the brain was extracted using the brain mask. RS-fMRI images were corrected for motion

381   using FLIRT. Principal component analysis (PCA) was applied to remove the unstructured

382   noise from the RS-MRI time course, followed by independent component analysis (ICA) with

383   the decomposition number of 200 using Multivariate Exploratory Linear Optimized

384   Decomposition into the Independent Components (MELODIC) module of the FSL software

385   package. Obtained components were classified as signal or noise (such as eye movement,

386   CSF pulsation, heart rate, and respiratory artifacts) based on the criteria as shown a previous

387   report (Griffanti et al., 2017), and noise components were regressed out from the rfMRI time

388   course using FSL tool (fsl_regfilt). All rfMRI images were finally normalized to the NIH template

389   using rfMRI-to-T2w and T2w-to-template transformation matrices obtained by FLIRT and

390   FNIRT, followed by spatial smoothing by Gaussian kernel with the full width of half maximum

391   value of 1.0 mm. The *ex-vivo* structure image was also normalized to the NIH template using

392   FLIRT and FNIRT.

393

394   *Cortico-subcortical functional networks in marmosets*

395   The group ICA analysis was first implemented for only cortical area 10 times with different

396   dimension numbers (from 16 to 25) to identify optimal dimensionality using MELODIC module

397   of the FSL software package – the 20 components solution was selected to be an appropriate

398   representative of meaningful components with reference to previous reports of marmoset

399   functional networks (Belcher et al., 2013; Ghahremani et al., 2016; Hori et al., 2019b). Second,

400   a spatial regression approach was used to obtain the temporal dynamics for each cortical

401   component within each scan's fMRI data sets (Filippini et al., 2009). In this process, the full set

402   of group-ICA spatial templates were used in a linear model fit against the separate fMRI data

403   sets. Finally, we calculated correlation coefficients between the time courses in each cortical

404   network and the time courses in each subcortical voxel using FSL's FEAT. The functional

405   connectivity maps (z-score maps) in the subcortical areas were then averaged across scans.

406   To assign each subcortical voxel to one of the networks, one network having the highest z-

407   value was assigned in each voxel.

408

409   *Cortico-subcortical functional networks in humans*

410   Human connectome project (HCP) datasets were used for human analysis (Van Essen et al.,

411   2013). RS-fMRI data for 100 subjects (4 scans for each subject, namely total 400 scans)

412   preprocessed with the HCP functional pipeline, including motion correction, distortion

413   correction, normalization to Montreal Neurological Institute (MNI) template space, and FMRIB's

414   ICA-based X-noiseifier (FIX) denoising (Salimi-Khorshidi et al., 2014) were downloaded from

415   the HCP website (https://www.humanconnectome.org/). Group ICA analysis was performed for

416   only cortical areas with 20 dimensions. After that, temporal dynamics for each cortical

417   component within each scan's data were obtained by a spatial regression approach using

418   group ICA templates, and correlation coefficients between the time courses in each cortical

419   network and the time courses in each subcortical voxel were calculated in the same way as in

420   the marmoset analysis. Finally, the functional connectivity maps (z-score maps) in the

421   subcortical areas were then averaged across scans.

422

423   *Subcortical volume of interest*

424   To identify the subcortical areas associated with each marmoset network, we applied the

425   subcortical atlas supplied by the NIH Marmoset Brain template (Liu et al., 2018), where the

426   thalamus is not parcellated into subthalamic nuclei. Based on the ex-vivo image normalized to

427   the NIH template, we created the subthalamic VOIs (anterior (AN), laterodorsal (LD),

428   mediodorsal (MD), ventral anterior (VA), ventral lateral (VL), ventral posterior (VP) and

429   pulvinar) with reference to the Paxinos atlas (Paxinos et al., 2012). For human subcortical

430   VOIs, standard mesh atlas for subcortical area supplied by HCP pipeline was used

431   (Atlas_ROIs_2.nii.gz), which does not have VOIs of subthalamic nuclei, lateral geniculate

432   nucleus (LGN), superior colliculus (SC) and inferior colliculus (IC). For thalamic nuclei, the

433   histological-based atlas supplied by NeuroImaging and Surgical Technologies Lab was used

434   (Xiao et al., 2015; Xiao et al., 2012). Also, a radiologist made the VOIs for LGN, SC and IC

435   based on the MNI T1w template.

436

437   *Comparison of subcortical connectivity profiles*

438   To determine whether the subcortical connectivity profiles are either similar or dissimilar from

439   each other, we used Manhattan distance among each connectivity fingerprint (Mars et al.,

440   2018; Mars et al., 2016). Connectivity fingerprints were created for marmosets and humans by

441   determining the mean z-values in seven target regions placed in the caudate, putamen,

442   hippocampus, amygdala, SC, IC, and LGN. We normalized the fingerprint to a range between

443   0 (weakest connection with any of the target areas) and 1 (strongest connection with any of the

444   target areas) to compare a pattern of connections with target areas, rather than absolute

445   strength. Permutation testing was used to test the significance of the match between each of

446   the marmoset and human subcortical network by calculating 10,000 different permutations of

447   the fingerprint target networks in marmosets. $p < 0.05$ is considered as significantly smaller

448   Manhattan distance than expected chance. This analysis was performed using custom tools

449   written in Matlab (the Mathworks, Natick, MA, USA).
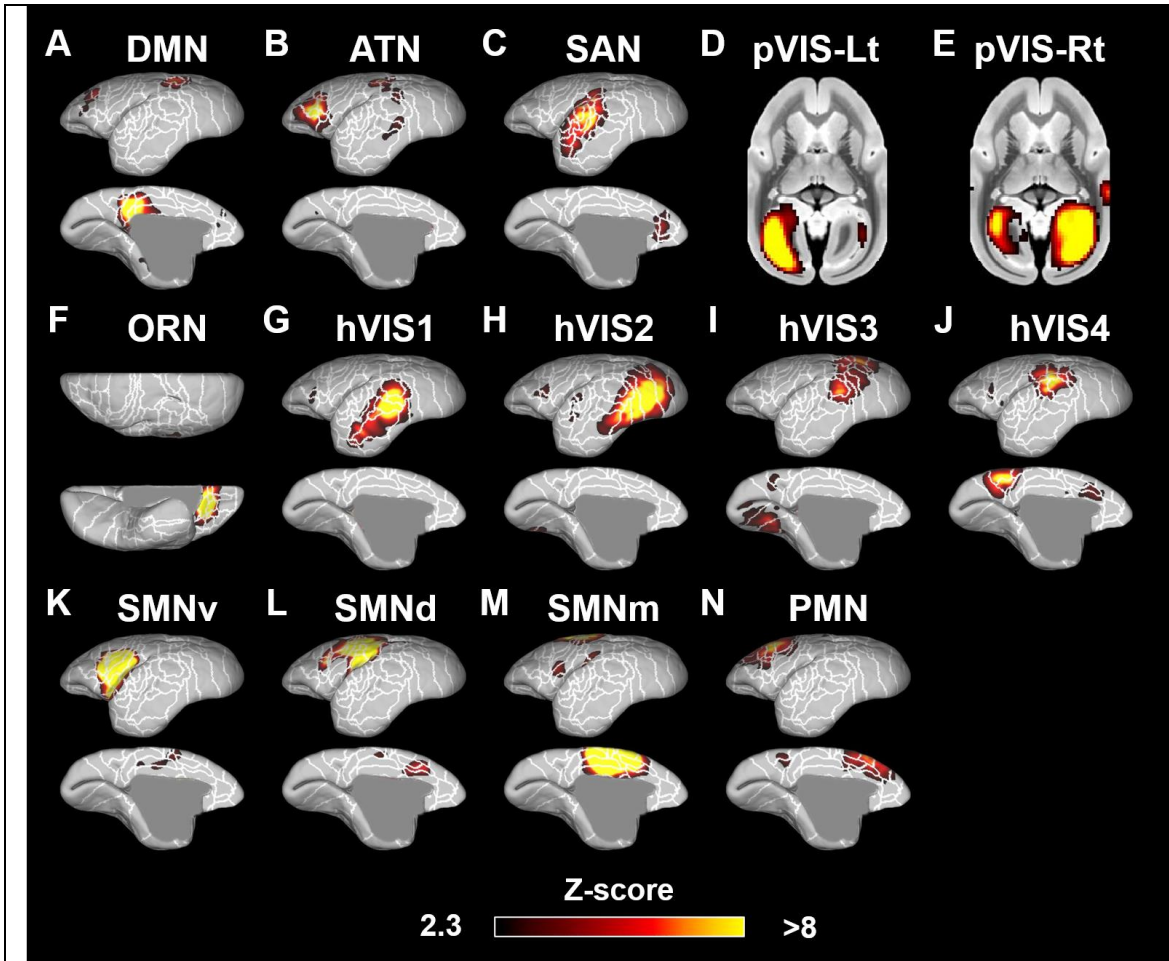
450

451 **Figures**

452

Figure 1. Fourteen components identified as resting-state networks in the marmosets. These networks were labeled based on previous studies (Belcher et al., 2013; Hori et al., 2020b) as follows: (A) default mode network (DMN); (B) attention network (ATN); (C) salience network (SAN); (D) left primary visual network (pVIS-Lt); (E) right primary VIS (pVIS-Rt); (F) orbitofrontal network (ORN); (G)-(J) high-order VIS (hVIS1-4); (K)-(M) somatomotor networks ventral (SMNv), dorsal (SMNd), and medial (SMNm); (N) premotor network (PMN). Color bar represents the z-score of these correlation patterns thresholding at 2.3. White lines show the cytoarchitectonic borders for reference (Liu et. al., 2018).

453

454
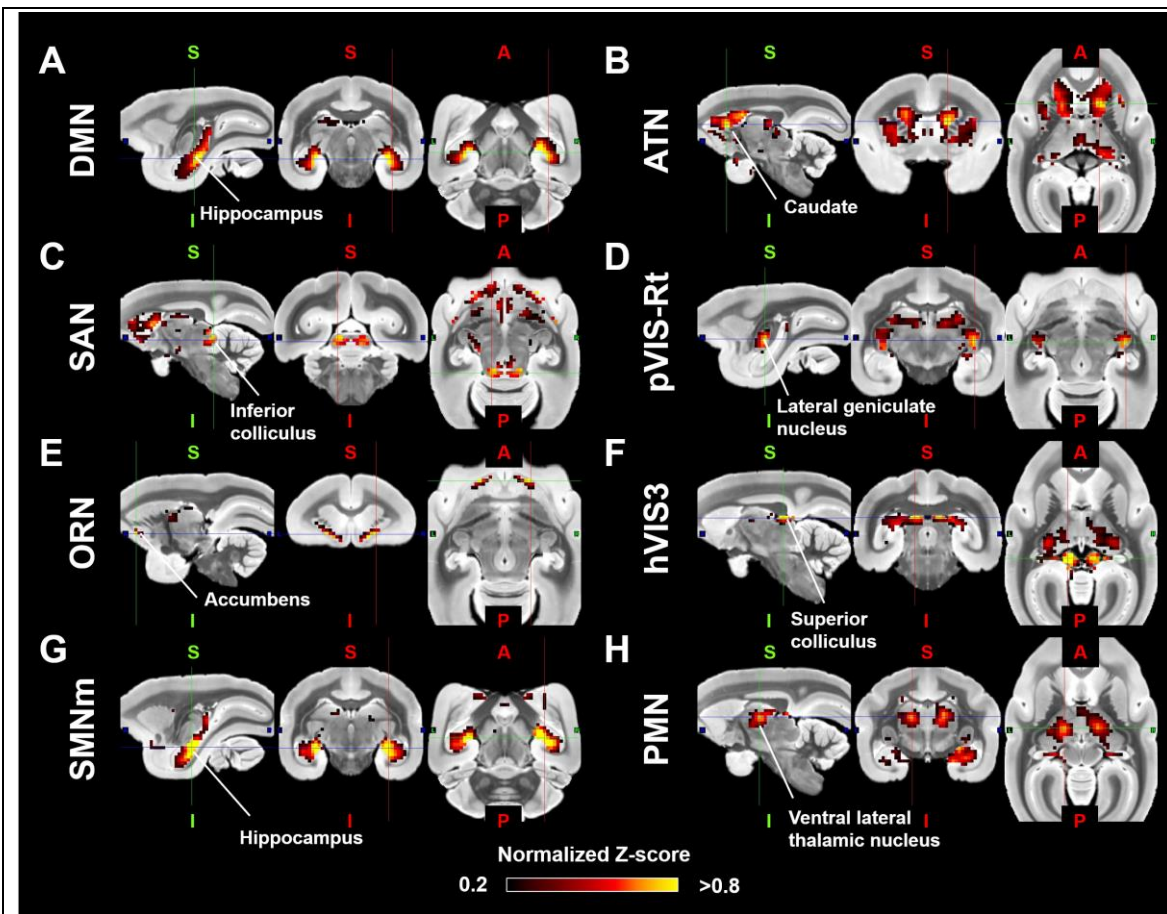
Figure 2. Representative subcortical z-score maps for each resting-state network (RSN). The z-score maps were normalized to be maximum z-value equal to 1, and were shown in sagittal, coronal, and axial slices deemed most representative of the activation patterns. (A) default mode network (DMN: corresponding to Fig. 1A); (B) attention network (ATN: corresponding to Fig. 1B); (C) salience network (SAN: corresponding to Fig. 1C); (D) primary visual network (pVIS: corresponding to Fig. 1E); (E) orbitofrontal network (ORN: corresponding to Fig. 1F); (F) high-order VIS (corresponding to Fig. 1I); (G) somatomotor network (SMN) medial sensory part (corresponding to Fig. 1M); (H) premotor network (PMN) (corresponding to Fig. 1N).

455

456
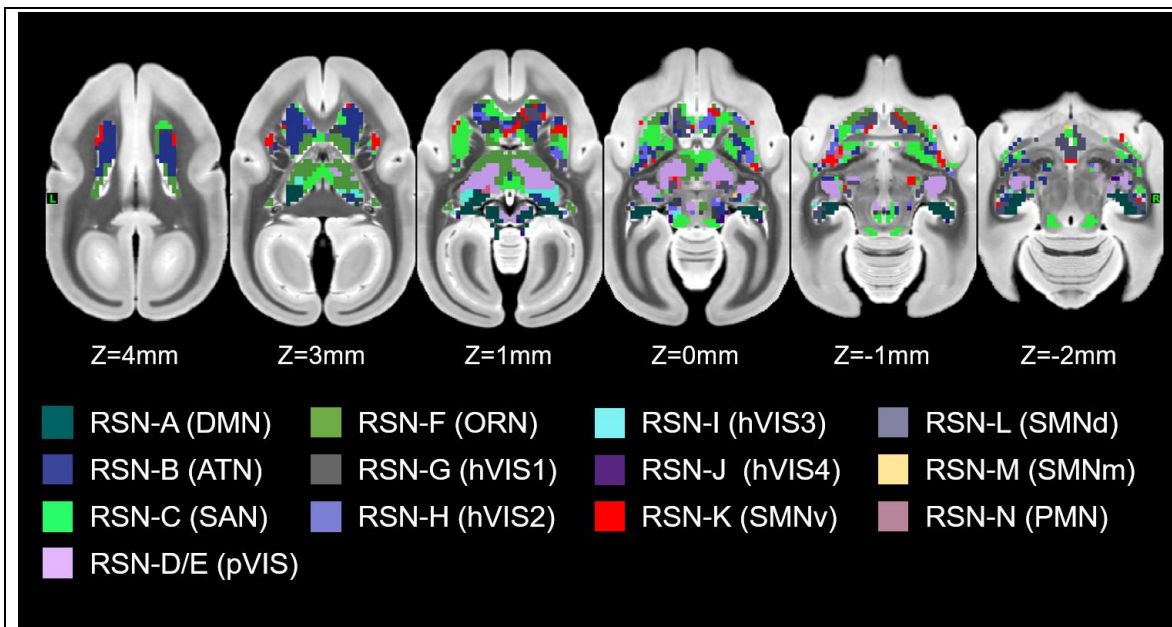
Figure 3. A parcellation of the marmoset subcortical area. The network with the highest z-value among all networks was assigned as the main network related to the voxel. The colors on the surfaces and volumes are corresponding to the name of networks in Figure 1.
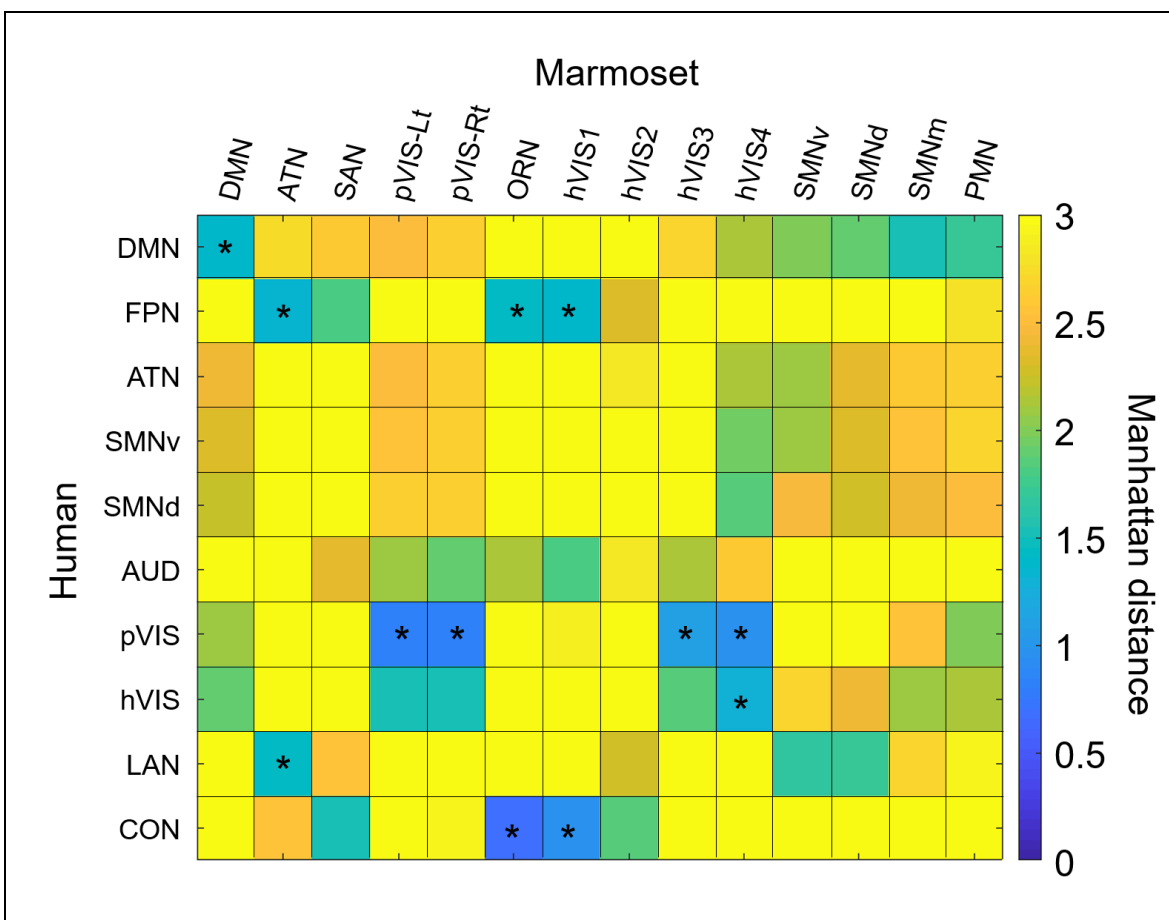
457

458

Figure 4. The similarity of subcortical network patterns between marmosets and humans. Manhattan distance between these species were plotted in matrix form. Significant similarities were marked by an asterisk within the matrix.
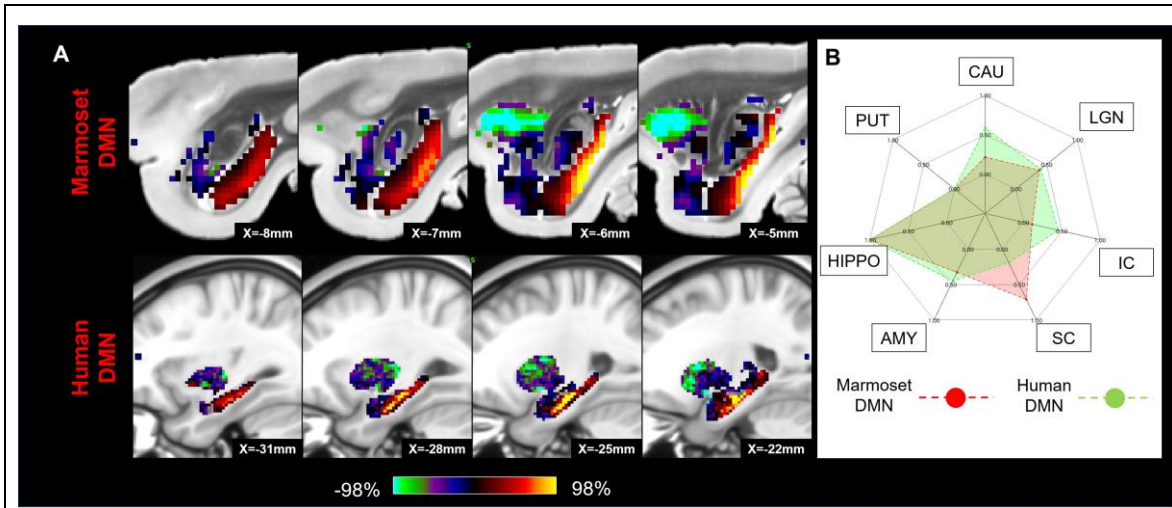
459

460

461

Figure 5. Matching human default mode network (DMN) to marmoset DMN in subcortical areas. (A) Z-score maps were shown in sagittal slices focused on the hippocampus, which has the strongest connections in both species. A single-color palette applies to all two species, but is scaled according to percentile ranges within each species rather than to absolute values. (B) A fingerprint shows the matching connectivity patterns between marmosets and humans. Red and green areas indicate marmoset and human fingerprints, respectively.

CAU: caudate; PUT: putamen; HIPPO: hippocampus; AMY: amygdala; SC: superior colliculus; IC: inferior colliculus; LGN: lateral geniculate nucleus.
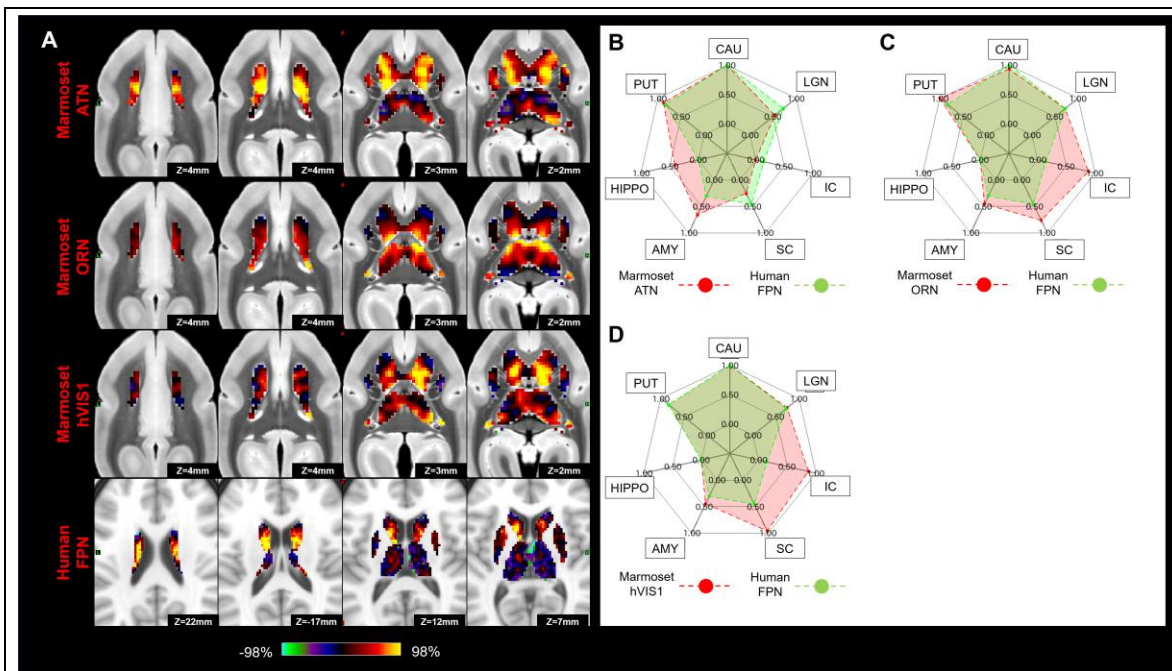
462

463

Figure 6. Matching human frontoparietal network (FPN) to marmoset attention (ATN), orbitofrontal (ORN), and high-order visual networks (hVIS1) in subcortical area. (A) Z-score maps were shown in axial slices focused on the caudate, which has the strongest connections in both species. A single-color palette applies to all two species, but is scaled according to percentile ranges within each species rather than to absolute values. (B-D) Fingerprints show the matching connectivity patterns between marmosets and humans. Red and green areas indicate marmoset and human fingerprints, respectively.

CAU: caudate; PUT: putamen; HIPPO: hippocampus; AMY: amygdala; SC: superior colliculus; IC: inferior colliculus; LGN: lateral geniculate nucleus.
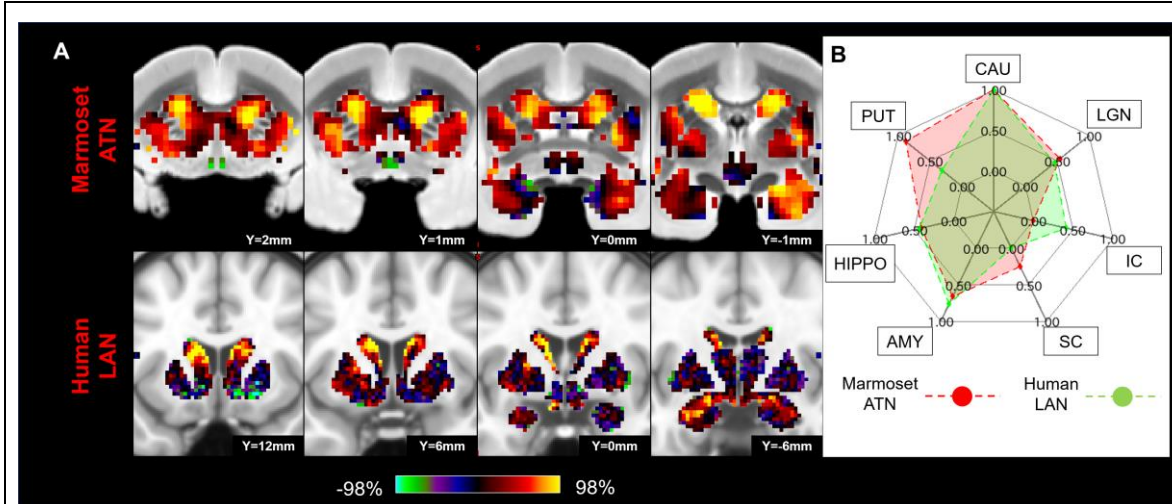
464

Figure 7. Matching human language network (LAN) to marmoset attention network (ATN) in subcortical area. (A) Z-score maps were shown in coronal slices focused on the caudate and amygdala, which have strong connections in both species. A single-color palette applies to all two species, but is scaled according to percentile ranges within each species rather than to absolute values. (B) Fingerprint shows the matching connectivity pattern between marmosets and humans. Red and green areas indicate marmoset and human fingerprints, respectively.

CAU: caudate; PUT: putamen; HIPPO: hippocampus; AMY: amygdala; SC: superior colliculus; IC: inferior colliculus; LGN: lateral geniculate nucleus.
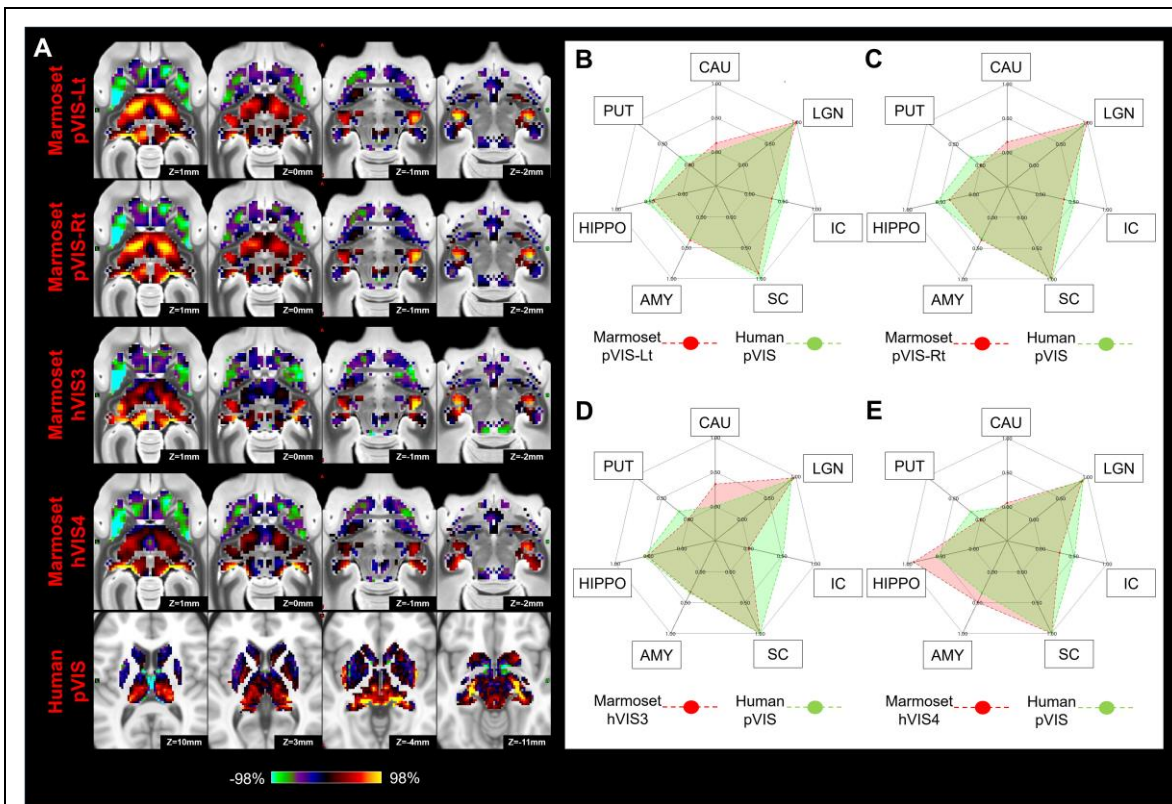
465

466

Figure 8. Matching human primary visual network (pVIS) to marmoset VISs (pVIS-Lt, pVIS-Rt, hVIS3, and hVIS4) in subcortical area. (A) Z-score maps for each were shown in axial slices focused on the superior colliculus and lateral geniculate nucleus, which have strong connections in both species. A single-color palette applies to all two species, but is scaled according to percentile ranges within each species rather than to absolute values. (B-E) Fingerprints show the matching connectivity patterns between marmosets and humans. Red and green areas indicate marmoset and human fingerprints, respectively.

CAU: caudate; PUT: putamen; HIPPO: hippocampus; AMY: amygdala; SC: superior colliculus; IC: inferior colliculus; LGN: lateral geniculate nucleus.
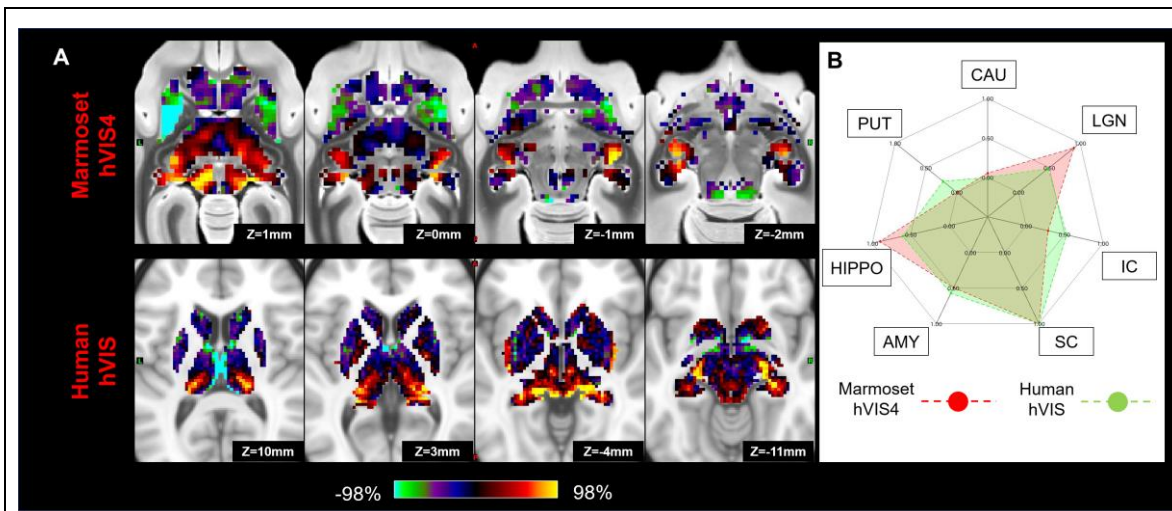
467

468

Figure 9. Matching human secondary visual network (hVIS) to marmoset high-order visual network (hVIS4) in subcortical area. (A) Z-score maps were shown in axial slices focused on the superior colliculus and lateral geniculate nucleus, which have strong connections in both species. A single-color palette applies to all two species, but is scaled according to percentile ranges within each species rather than to absolute values. (B) A fingerprint shows the matching connectivity patterns between marmosets and humans. Red and green areas indicate marmoset and human fingerprints, respectively.

CAU: caudate; PUT: putamen; HIPPO: hippocampus; AMY: amygdala; SC: superior colliculus; IC: inferior colliculus; LGN: lateral geniculate nucleus.
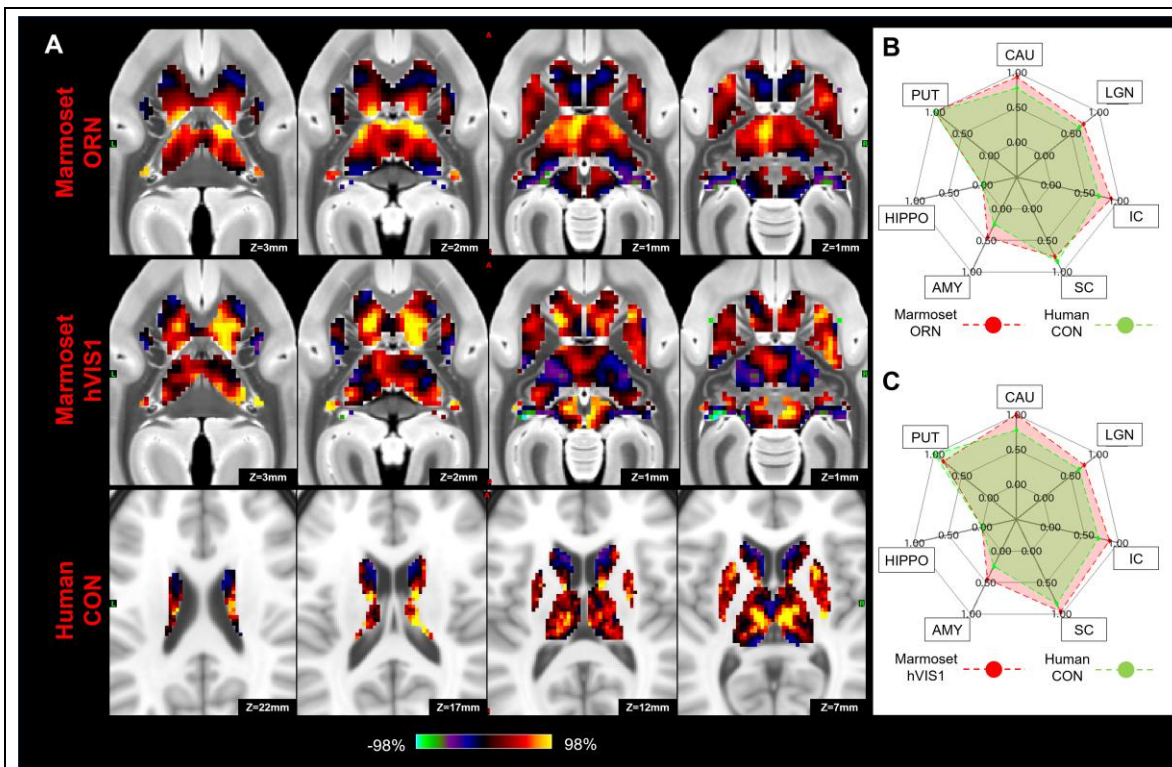
469

470

Figure 10. Matching human cingulo-opercular network (CON) to marmoset orbitofrontal (ORN) and high-order visual networks (hVIS1) in subcortical area. (A) Z-score maps were shown in axial slices focused on the caudate and putamen, which have strong connections in both species. A single-color palette applies to all two species, but is scaled according to percentile ranges within each species rather than to absolute values. (B, C) Fingerprints show the matching connectivity patterns between marmosets and humans. Red and green areas indicate marmoset and human fingerprints, respectively.

CAU: caudate; PUT: putamen; HIPPO: hippocampus; AMY: amygdala; SC: superior colliculus; IC: inferior colliculus; LGN: lateral geniculate nucleus.

471

472   **Supplementary Figure**

473
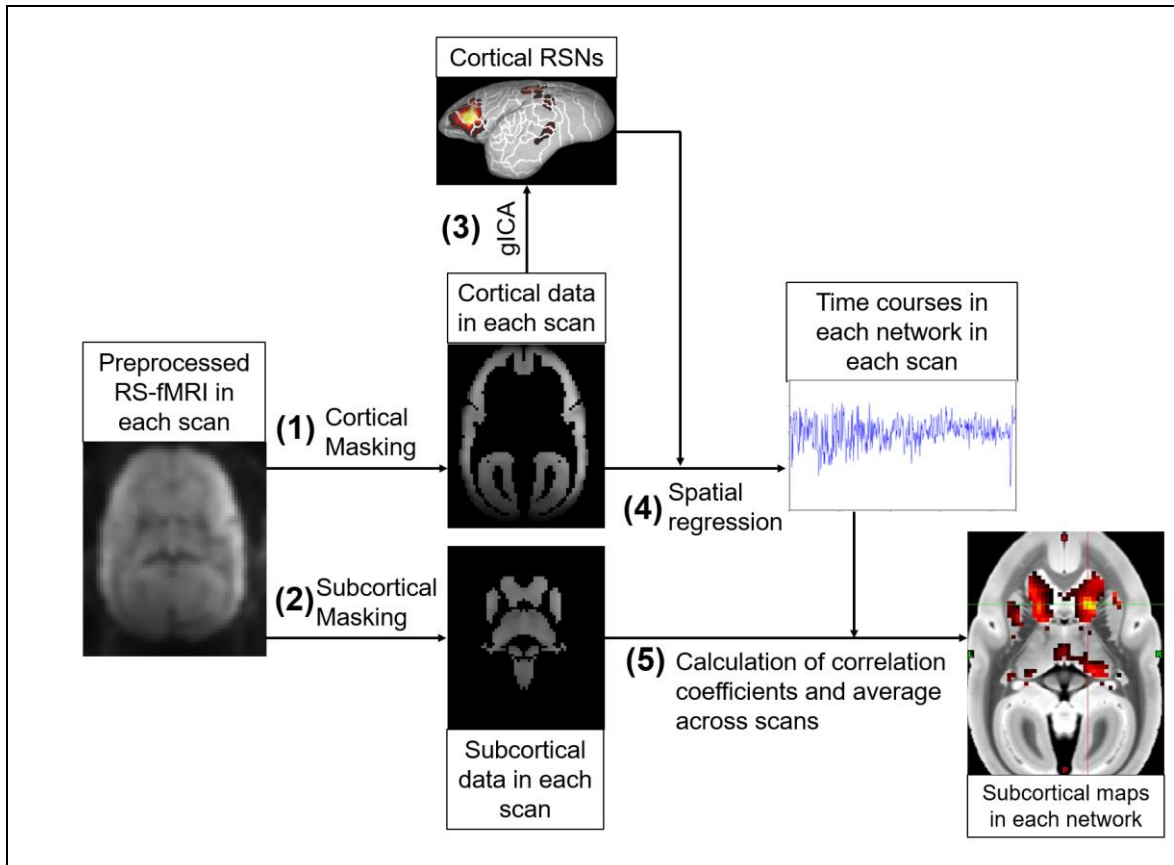
Supplementary Figure 1. Flow chart of analysis to calculate the subcortical connectivity maps. Each RS-fMRI scan was preprocessed, and (1) cortical and (2) subcortical regions were extracted using masks. (3) Using all cortical RS-fMRI datasets, group ICA (gICA) was performed so that 14 and 10 cortical resting-state networks (RSNs) were identified for marmosets and humans, respectively. (4) The time courses of each network in each scan were calculated using spatial regression technique and obtained cortical RSNs, (5) then correlation coefficients between the time courses in each cortical network and the time courses in each subcortical voxel were calculated. Obtained correlation coefficient maps in each network were averaged across scans.

474

475

476
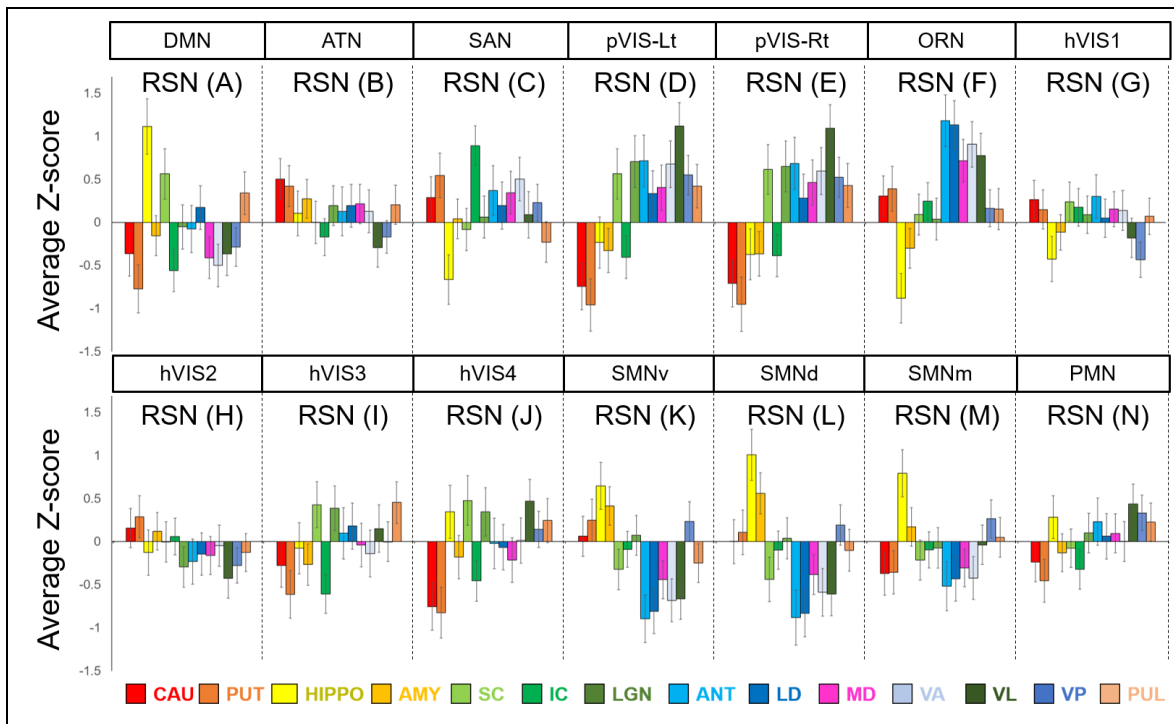
Supplementary Figure2. Mean z-score values in each subcortical area in each marmoset resting-state network (RSN). The error bars represent the standard error of the mean. The RSNs described here are corresponding to those in Fig. 1. CAU: caudate; PUT: putamen; HIPPO: hippocampus; AMY: amygdala; SC: superior colliculus; IC: inferior colliculus; LGN: lateral geniculate nucleus; ANT: anterior part of thalamic nucleus; LD: laterodorsal thalamic nucleus; MD: mediodorsal thalamic nucleus; VA: ventral anterior thalamic nucleus; VL: ventral lateral thalamic nucleus; VP: ventral posterior thalamic nucleus; PUL: pulvinar nucleus.

477

478

479
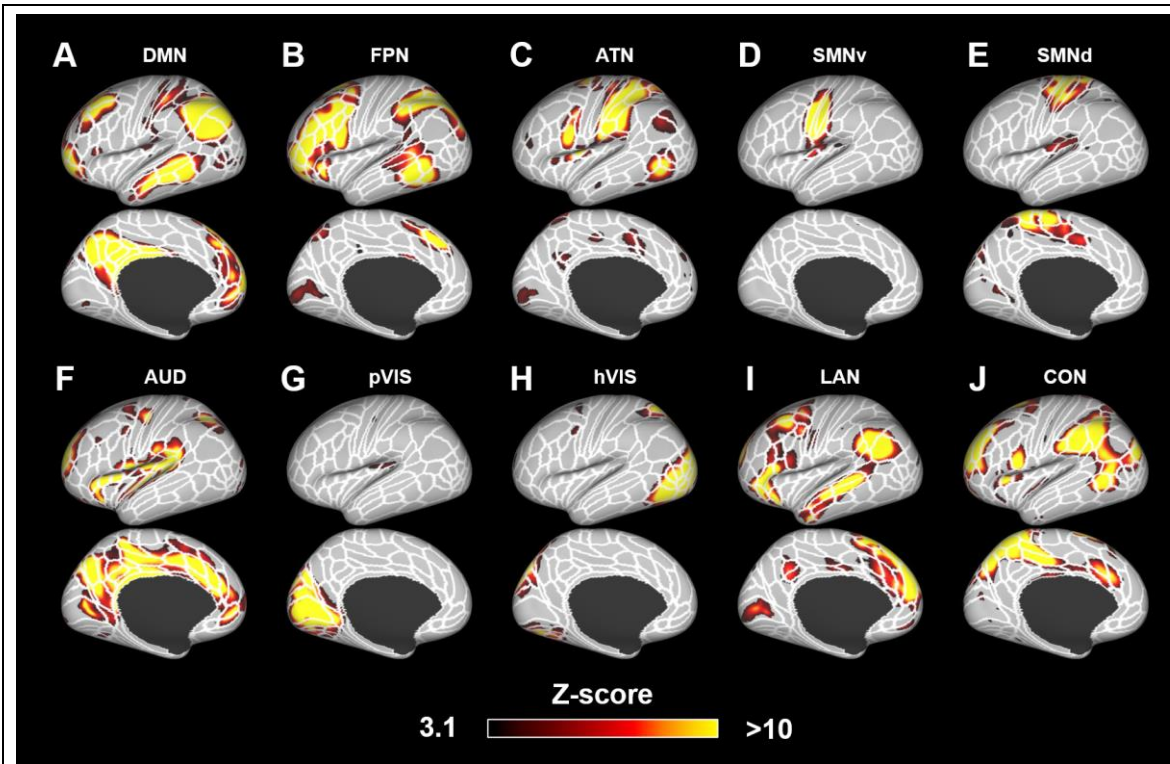
Supplementary Figure 3. Ten components identified as resting-state networks in humans. These networks were labeled based on a previous study (Ji et. al., 2019) as follows: (A) default mode network (DMN); (B) frontoparietal network (FPN); (C) attention network (ATN); (D) somatomotor network ventral part (SMN1); (E) SMN dorsomedial part (SMN2); (F) auditory network (AUD); (G) primary visual network (pVIS); (H) high-order VIS (hVIS); (I) language network (LAN); (J) cingulo-opercular network (CON). Color bar represents the z-score of these correlation patterns thresholding at 3.1. White lines show the parcellation borders created based on the multimodal magnetic resonance images from Human Connectome Project (Glasser et al., 2016).

480

481

482
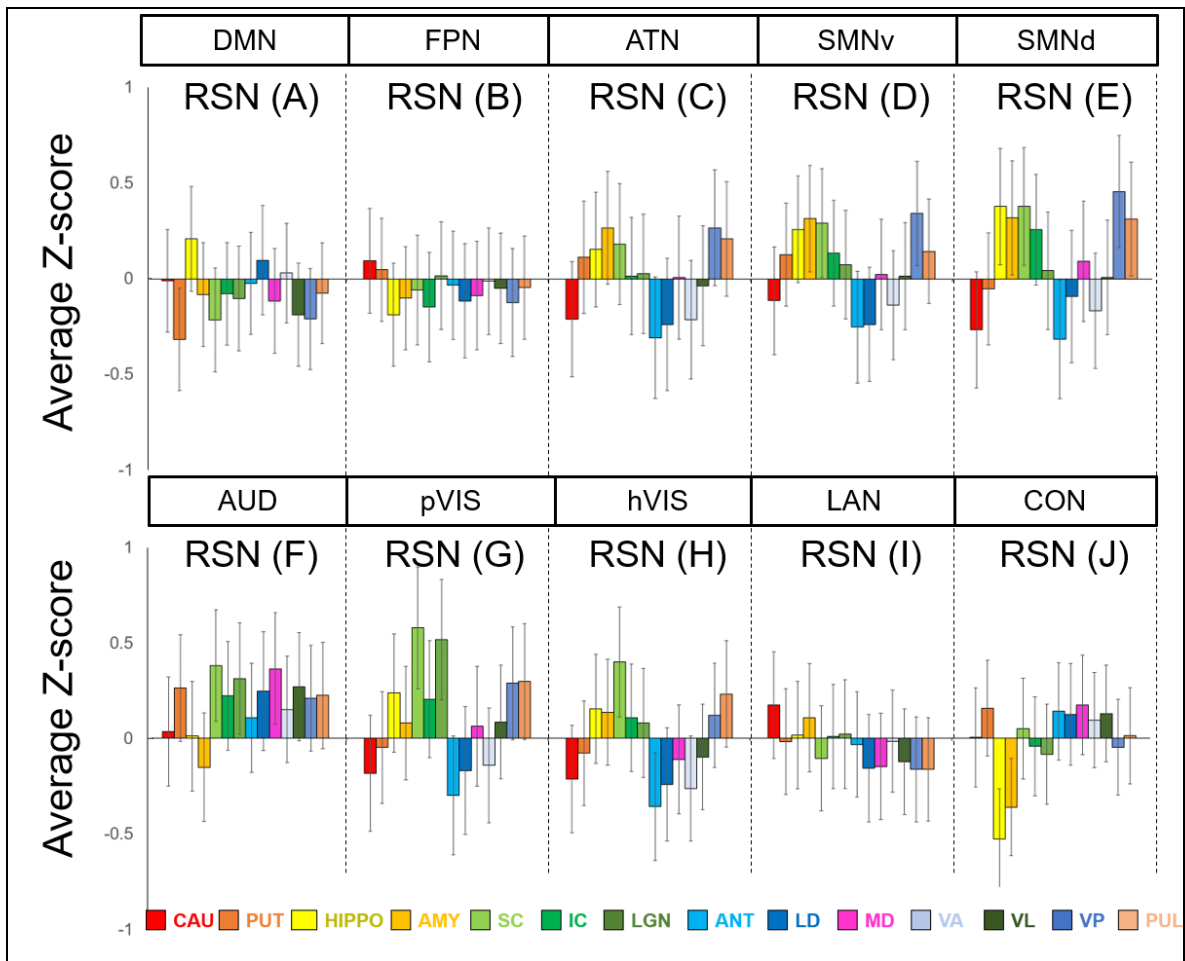
Supplementary Figure 4. Mean z-score values in each subcortical area in each human resting-state network (RSN). The error bars represent the standard error of the mean. The RSNs described here are corresponding to those in Supplementary fig. 2. CAU: caudate; PUT: putamen; HIPPO: hippocampus; AMY: amygdala; SC: superior colliculus; IC: inferior colliculus; LGN: lateral geniculate nucleus; ANT: anterior part of thalamic nucleus; LD: laterodorsal thalamic nucleus; MD: mediodorsal thalamic nucleus; VA: ventral anterior thalamic nucleus; VL: ventral lateral thalamic nucleus; VP: ventral posterior thalamic nucleus; PUL: pulvinar nucleus.

483

484

Reference

Abe H, Tani T, Mashiko H, Kitamura N, Hayami T, Watanabe S, Sakai K, Suzuki W, Mizukami H, Watakabe A, Yamamori T, Ichinohe N. 2018. Axonal Projections From the Middle Temporal Area in the Common Marmoset. *Frontiers in Neuroanatomy* **12**:89 doi:10.3389/fnana.2018.00089

Balsters JH, Zerbi V, Sallet J, Wenderoth N, Mars RB. 2020. Primate homologs of mouse cortico-striatal circuits. *eLife* **9**:e53680. doi:10.7554/eLife.53680

Beckmann CF, Smith SM. 2004. Probabilistic Independent Component Analysis for Functional Magnetic Resonance Imaging. *IEEE Trans Med Imaging* **23**:137–152. doi:10.1109/TMI.2003.822821

Belcher AM, Yen CC, Stepp H, Gu H, Lu H, Yang Y, Silva AC, Stein EA. 2013. Large-Scale Brain Networks in the Awake, Truly Resting Marmoset Monkey. *Journal of Neuroscience* **33**:16796–16804. doi:10.1523/JNEUROSCI.3146-13.2013

Brysch W, Brysch I, Creutzfeldt OD, Schlingensiepen R. 1990. The topology of the thalamo-cortical projections in the marmoset monkey (CMlithrixjacchus). *Experimental Brain Research* 17.

Burman KJ, Bakola S, Richardson KE, Yu H-H, Reser DH, Rosa MGP. 2015. Cortical and thalamic projections to cytoarchitectural areas 6Va and 8C of the marmoset monkey: Connectionally distinct subdivisions of the lateral premotor cortex: connections of marmoset lateral premotor cortex. *Journal of Comparative Neurology* **523**:1222–1247. doi:10.1002/cne.23734

Cléry JC, Schaeffer DJ, Hori Y, Gilbert KM, Hayrynen LK, Gati JS, Menon RS, Everling S. 2020. Looming and receding visual networks in awake marmosets investigated with fMRI. *NeuroImage* **215**:116815. doi:10.1016/j.neuroimage.2020.116815

Corbetta M, Akbudak E, Conturo TE, Snyder AZ, Ollinger JM, Drury HA, Linenweber MR, Petersen SE, Raichle ME, Van Essen DC, Shulman GL. 1998. A Common Network of Functional Areas for Attention and Eye Movements. *Neuron* **21**:761–773. doi:10.1016/S0896-6273(00)80593-0

514 Dosenbach NUF, Fair DA, Miezin FM, Cohen AL, Wenger KK, Dosenbach RAT, Fox MD, Snyder
515   AZ, Vincent JL, Raichle ME, Schlaggar BL, Petersen SE. 2007. Distinct brain networks
516   for adaptive and stable task control in humans. *Proceedings of the National Academy of
517   Sciences* **104**:11073–11078. doi:10.1073/pnas.0704320104

518 Dosenbach NUF, Visscher KM, Palmer ED, Miezin FM, Wenger KK, Kang HC, Burgund ED,
519   Grimes AL, Schlaggar BL, Petersen SE. 2006. A Core System for the Implementation of
520   Task Sets. *Neuron* **50**:799–812. doi:10.1016/j.neuron.2006.04.031

521 Filippini N, MacIntosh BJ, Hough MG, Goodwin GM, Frisoni GB, Smith SM, Matthews PM,
522   Beckmann CF, Mackay CE. 2009. Distinct patterns of brain activity in young carriers of
523   the APOE- 4 allele. *Proceedings of the National Academy of Sciences* **106**:7209–7214.
524   doi:10.1073/pnas.0811879106

525 Ghahremani M, Hutchison RM, Menon RS, Everling S. 2016. Frontoparietal Functional
526   Connectivity in the Common Marmoset. *Cerebral Cortex* **27**:3890–3905.
527   doi:10.1093/cercor/bhw198

528 Ghahremani M, Johnston KD, Ma L, Hayrynen LK, Everling S. 2019. Electrical microstimulation
529   evokes saccades in posterior parietal cortex of common marmosets. *Journal of
530   Neurophysiology* **122**:1765–1776. doi:10.1152/jn.00417.2019

531 Glasser MF, Coalson TS, Robinson EC, Hacker CD, Harwell J, Yacoub E, Ugurbil K, Andersson
532   J, Beckmann CF, Jenkinson M, Smith SM, Van Essen DC. 2016. A multi-modal
533   parcellation of human cerebral cortex. *Nature* **536**:171–178. doi:10.1038/nature18933

534 Greicius MD, Srivastava G, Reiss AL, Menon V. 2004. Default-mode network activity
535   distinguishes Alzheimer's disease from healthy aging: Evidence from functional MRI.
536   *Proceedings of the National Academy of Sciences* **101**:4637–4642.
537   doi:10.1073/pnas.0308627101

538 Griffanti L, Douaud G, Bijsterbosch J, Evangelisti S, Alfaro-Almagro F, Glasser MF, Duff EP,
539   Fitzgibbon S, Westphal R, Carone D, Beckmann CF, Smith SM. 2017. Hand classification
540   of fMRI ICA noise components. *NeuroImage* **154**:188–205.
541   doi:10.1016/j.neuroimage.2016.12.036

542 Handler WB, Bindseil G, Chaddock R, Dalrymple B, Gati JS, Gilbert KM, Harris C, Klassen LM,
543   Peterson J, Van Sas F, Chronik BA. 2020. Design and construction of a gradient coil for
544   high resolution marmoset imaging. *Biomedical Physics and Engineering Express*.
545   doi:10.1088/2057-1976/ab8d97

546 Hikosaka O, Wurtz RH. 1989. The basal ganglia. Reviews of Oculomotor Research **3**:257-281

547 Hori Y, Schaeffer DJ, Gilbert KM, Hayrynen LK, Cléry JC, Gati JS, Menon RS, Everling S. 2020a.
548   Comparison of resting-state functional connectivity in marmosets with tracer-based
549   cellular connectivity. *NeuroImage* **204**:116241. doi:10.1016/j.neuroimage.2019.116241

550 Hori Y, Schaeffer DJ, Gilbert KM, Hayrynen LK, Cléry JC, Gati JS, Menon RS, Everling S. 2020b.
551   Altered Resting-State Functional Connectivity Between Awake and Isoflurane
552   Anesthetized Marmosets. *Cerebral Cortex* bhaa168. doi:10.1093/cercor/bhaa168

553 Hung CC, Yen CC, Ciuchta JL, Papoti D, Bock NA, Leopold DA, Silva AC. 2015a. Functional
554   MRI of visual responses in the awake, behaving marmoset. *NeuroImage* **120**:1–11.
555   doi:10.1016/j.neuroimage.2015.06.090

556 Hung CC, Yen CC, Ciuchta JL, Papoti D, Bock NA, Leopold DA, Silva AC. 2015b. Functional
557   Mapping of Face-Selective Regions in the Extrastriate Visual Cortex of the Marmoset.
558   *Journal of Neuroscience* **35**:1160–1172. doi:10.1523/JNEUROSCI.2659-14.2015

559 Hutchison RM, Gallivan JP, Culham JC, Gati JS, Menon RS, Everling S. 2012. Functional
560   connectivity of the frontal eye fields in humans and macaque monkeys investigated with
561   resting-state   fMRI.   *Journal   of   Neurophysiology*   **107**:2463–2474.
562   doi:10.1152/jn.00891.2011

563 Ji JL, Spronk M, Kulkarni K, Repovš G, Anticevic A, Cole MW. 2019. Mapping the human brain's
564   cortical-subcortical   functional   network   organization.   *NeuroImage*   **185**:35–57.
565   doi:10.1016/j.neuroimage.2018.10.006

566 Johnston KD, Barker K, Schaeffer L, Schaeffer DJ, Everling S. 2018. Methods for chair
567   restraint and training of the common marmoset on oculomotor tasks. *J. Neurophysiol.*
568   **119**:1636–1646. doi: 10.1152/jn.00866.2017.

569   Kaas JH, Lyon DC. 2007. Pulvinar contributions to the dorsal and ventral streams of visual
570   processing in primates. *Brain Research Reviews* **55**:285–296.
571   doi:10.1016/j.brainresrev.2007.02.008

572   Li X, Morgan PS, Ashburner J, Smith J, Rorden C. 2016. The first step for neuroimaging data
573   analysis: DICOM to NIfTI conversion. *Journal of Neuroscience Methods* **264**:47–56.
574   doi:10.1016/j.jneumeth.2016.03.001

575   Liu C, Ye FQ, Newman JD, Szczupak D, Tian X, Yen CC-C, Majka P, Glen D, Rosa MGP, Leopold
576   DA, Silva AC. 2020. A resource for the detailed 3D mapping of white matter pathways in
577   the marmoset brain. *Nature Neurosci*ence **23**:271-80 doi:10.1038/s41593-019-0575-0

578   Liu C, Ye FQ, Yen CC-C, Newman JD, Glen D, Leopold DA, Silva AC. 2018. A digital 3D atlas of
579   the marmoset brain based on multi-modal MRI. *NeuroImage* **169**:106–116.
580   doi:10.1016/j.neuroimage.2017.12.004

581   Lu H, Zou Q, Gu H, Raichle ME, Stein EA, Yang Y. 2012. Rat brains also have a default mode
582   network. *Proceedings of the National Academy of Sciences* **109**:3979–3984.
583   doi:10.1073/pnas.1200506109

584   Luna B, Thulborn K, Strojwas M, McCurtain B, Berman R, Genovese C, Sweeney J. 1998. Dorsal
585   cortical regions subserving visually guided saccades in humans: an fMRI study. *Cerebral
586   Cortex* **8**:40–47. doi:10.1093/cercor/8.1.40

587   Ma L, Selvanayagam J, Ghahremani M, Hayrynen LK, Johnston KD, Everling S. 2020. Single-
588   unit activity in marmoset posterior parietal cortex in a gap saccade task. *Journal of
589   Neurophysiology* **123**:896–911. doi:10.1152/jn.00614.2019

590   Majka P, Bai S, Bakola S, Bednarek S, Chan JM, Jermakow N, Passarelli L, Reser DH, Theodoni
591   P, Worthy KH, Wang X-J, Wójcik DK, Mitra PP, Rosa MGP. 2020. Open access resource
592   for cellular-resolution analyses of corticocortical connectivity in the marmoset monkey.
593   *Nature Communications* **11**:1133. doi:10.1038/s41467-020-14858-0

594   Majka P, Chaplin TA, Yu H-H, Tolpygo A, Mitra PP, Wójcik DK, Rosa MGP. 2016. Towards a
595   comprehensive atlas of cortical connections in a primate brain: Mapping tracer injection
596   studies of the common marmoset into a reference digital template: Atlas of primate brain

597 cortical connections. *Journal of Comparative Neurology* **524**:2161–2181.

598 doi:10.1002/cne.24023

599 Mantini D, Gerits A, Nelissen K, Durand J-B, Joly O, Simone L, Sawamura H, Wardak C, Orban

600 GA, Buckner RL. 2011. Default mode of brain function in monkeys. *Journal of*

601 *Neuroscience* **31**:12954–12962.

602 Mars RB, Passingham RE, Jbabdi S. 2018. Connectivity Fingerprints: From Areal Descriptions

603 to Abstract Spaces. *Trends in Cognitive Sciences* **22**:1026–1037.

604 doi:10.1016/j.tics.2018.08.009

605 Mars RB, Verhagen L, Gladwin TE, Neubert F-X, Sallet J, Rushworth MFS. 2016. Comparing

606 brains by matching connectivity profiles. *Neuroscience & Biobehavioral Reviews* **60**:90–

607 97. doi:10.1016/j.neubiorev.2015.10.008

608 McDonald JS, Clifford CWG, Solomon SS, Chen SC, Solomon SG. 2014. Integration and

609 segregation of multiple motion signals by neurons in area MT of primate. *Journal of*

610 *Neurophysiology* **111**:369–378. doi:10.1152/jn.00254.2013

611 Miller CT, Thomas AW, Nummela SU, de la Mothe LA. 2015. Responses of primate frontal cortex

612 neurons during natural vocal communication. *Journal of Neurophysiology* **114**:1158–

613 1171. doi:10.1152/jn.01003.2014

614 Mitchell JF, Leopold DA. 2015. The marmoset monkey as a model for visual neuroscience.

615 *Neuroscience Research* **93**:20–46. doi:10.1016/j.neures.2015.01.008

616 Okano H, Mitra P. 2015. Brain-mapping projects using the common marmoset. *Neuroscience*

617 *Research* **93**:3–7. doi:10.1016/j.neures.2014.08.014

618 Okano H, Sasaki E, Yamamori T, Iriki A, Shimogori T, Yamaguchi Y, Kasai K, Miyawaki A. 2016.

619 Brain/MINDS: A Japanese National Brain Project for Marmoset Neuroscience. *Neuron*

620 **92**:582–590. doi:10.1016/j.neuron.2016.10.018

621 Park JE, Zhang XF, Choi S-H, Okahara J, Sasaki E, Silva AC. 2016. Generation of transgenic

622 marmosets expressing genetically encoded calcium indicators. *Scientific Reports* **6**.

623 doi:10.1038/srep34931

624 Passingham RE, Stephan KE, Kötter R. 2002. The anatomical basis of functional localization in

625 the cortex. *Nature Reviews Neuroscience* **3**:606–616. doi:10.1038/nrn893

626 Paxinos G., Watson C., Petrides M., Rosa M., Tokuno H. 2012. The Marmoset Brain in
627   Stereotaxic Coordinates. Academic Press http://hdl.handle.net/20.500.11937/40725.

628 Phillips JM, Everling S. 2012. Neural Activity in the Macaque Putamen Associated with Saccades
629   and Behavioral Outcome. *PLoS ONE* **7**:e51596. doi:10.1371/journal.pone.0051596

630 Raemaekers M, Jansma JM, Cahn W, Van der Geest JN, van der Linden JA, Kahn RS, Ramsey
631   NF. 2002. Neuronal Substrate of the Saccadic Inhibition Deficit in Schizophrenia
632   Investigated With 3-Dimensional Event-Related Functional Magnetic Resonance
633   Imaging. *Archives of General Psychiatry* **59**:313–320. doi:10.1001/archpsyc.59.4.313

634 Raemaekers M, Ramsey NF, Vink M, van den Heuvel MP, Kahn RS. 2006. Brain Activation
635   During Antisaccades in Unaffected Relatives of Schizophrenic Patients. *Biological*
636   *Psychiatry* **59**:530–535. doi:10.1016/j.biopsych.2005.07.030

637 Reser DH, Burman KJ, Yu H-H, Chaplin TA, Richardson KE, Worthy KH, Rosa MGP. 2013.
638   Contrasting Patterns of Cortical Input to Architectural Subdivisions of the Area 8
639   Complex: A Retrograde Tracing Study in Marmoset Monkeys. *Cerebral Cortex* **23**:1901–
640   1922. doi:10.1093/cercor/bhs177

641 Salimi-Khorshidi G, Douaud G, Beckmann CF, Glasser MF, Griffanti L, Smith SM. 2014.
642   Automatic denoising of functional MRI data: Combining independent component analysis
643   and hierarchical fusion of classifiers. *NeuroImage* **90**:449–468.
644   doi:10.1016/j.neuroimage.2013.11.046

645 Sasaki E, Suemizu H, Shimada A, Hanazawa K, Oiwa R, Kamioka M, Tomioka I, Sotomaru Y,
646   Hirakawa R, Eto T, Shiozawa S, Maeda T, Ito M, Ito R, Kito C, Yagihashi C, Kawai K,
647   Miyoshi H, Tanioka Y, Tamaoki N, Habu S, Okano H, Nomura T. 2009. Generation of
648   transgenic non-human primates with germline transmission. *Nature* **459**:523–527.
649   doi:10.1038/nature08090

650 Schaeffer DJ, Adam R, Gilbert KM, Gati JS, Li AX, Menon RS, Everling S. 2017. Diffusion-
651   weighted tractography in the common marmoset monkey at 9.4T. *Journal of*
652   *Neurophysiology* **118**:1344–1354. doi:10.1152/jn.00259.2017

653   Schaeffer DJ, Gilbert KM, Gati JS, Menon RS, Everling S. 2019a. Intrinsic Functional Boundaries
654   of Lateral Frontal Cortex in the Common Marmoset Monkey. *The Journal of*
655   *Neuroscience* **39**:1020–1029. doi:10.1523/JNEUROSCI.2595-18.2018

656   Schaeffer DJ, Gilbert KM, Ghahremani M, Gati JS, Menon RS, Everling S. 2019b. Intrinsic
657   functional clustering of anterior cingulate cortex in the common marmoset. *NeuroImage*
658   **186**:301–307. doi:10.1016/j.neuroimage.2018.11.005

659   Schaeffer DJ, Gilbert KM, Hori Y, Gati JS, Menon RS, Everling S. 2019c. Integrated
660   radiofrequency array and animal holder design for minimizing head motion during awake
661   marmoset functional magnetic resonance imaging. *NeuroImage* **193**:126–138.
662   doi:10.1016/j.neuroimage.2019.03.023

663   Schaeffer DJ, Gilbert KM, Hori Y, Hayrynen LK, Johnston KD, Gati JS, Menon RS, Everling S.
664   2019d. Task-based fMRI of a free-viewing visuo-saccadic network in the marmoset
665   monkey. *NeuroImage* **202**:116147. doi:10.1016/j.neuroimage.2019.116147

666   Schaeffer DJ, Hori Y, Gilbert KM, Gati JS, Menon RS, Everling S. 2020. Divergence of rodent
667   and primate medial frontal cortex functional connectivity. *Proceedings of the National*
668   *Academy of Sciences in press*

669   Selvanayagam J, Johnston KD, Schaeffer DJ, Hayrynen LK, Everling S. 2019. Functional
670   Localization of the Frontal Eye Fields in the Common Marmoset Using Microstimulation.
671   *Journal of Neuroscience* **39**:9197–9206. doi:10.1523/JNEUROSCI.1786-19.2019

672   Sheffield JM, Repovs G, Harms MP, Carter CS, Gold JM, MacDonald III AW, Daniel Ragland J,
673   Silverstein SM, Godwin D, Barch DM. 2015. Fronto-parietal and cingulo-opercular
674   network integrity and cognition in health and schizophrenia. *Neuropsychologia* **73**:82–
675   93. doi:10.1016/j.neuropsychologia.2015.05.006

676   Silva AC, Liu JV, Hirano Y, Leoni RF, Merkle H, Mackel JB, Zhang XF, Nascimento GC,
677   Stefanovic B. 2011. Longitudinal functional magnetic resonance imaging in animal
678   models. *Methods Mol Biol.* **711**:281–302.

679   Smith SM. 2002. Fast robust automated brain extraction. *Human Brain Mapping* **17**:143–155.
680   doi:10.1002/hbm.10062

681 Smith SM, Jenkinson M, Woolrich MW, Beckmann CF, Behrens TEJ, Johansen-Berg H,
682   Bannister PR, De Luca M, Drobnjak I, Flitney DE, Niazy RK, Saunders J, Vickers J,
683   Zhang Y, De Stefano N, Brady JM, Matthews PM. 2004. Advances in functional and
684   structural MR image analysis and implementation as FSL. *NeuroImage* **23**:S208–S219.
685   doi:10.1016/j.neuroimage.2004.07.051

686 Solomon SG, Rosa MGP. 2014. A simpler primate brain: the visual system of the marmoset
687   monkey. *Frontiers in Neural Circuits* **8**:96 doi:10.3389/fncir.2014.00096

688 Thomas Yeo BT, Krienen FM, Sepulcre J, Sabuncu MR, Lashkari D, Hollinshead M, Roffman JL,
689   Smoller JW, Zöllei L, Polimeni JR, Fischl B, Liu H, Buckner RL. 2011. The organization
690   of the human cerebral cortex estimated by intrinsic functional connectivity. *Journal of*
691   *Neurophysiology* **106**:1125–1165. doi:10.1152/jn.00338.2011

692 Tomioka I, Ishibashi H, Minakawa EN, Motohashi HH, Takayama O, Saito Y, Popiel HA, Puentes
693   S, Owari K, Nakatani T, Nogami N, Yamamoto K, Noguchi S, Yonekawa T, Tanaka Y,
694   Fujita N, Suzuki H, Kikuchi H, Aizawa S, Nagano S, Yamada D, Nishino I, Ichinohe N,
695   Wada K, Kohsaka S, Nagai Y, Seki K. 2017a. Transgenic Monkey Model of the
696   Polyglutamine Diseases Recapitulating Progressive Neurological Symptoms. *eNeuro*
697   **4**:1–16. doi:10.1523/ENEURO.0250-16.2017

698 Tomioka I, Nogami N, Nakatani T, Owari K, Fujita N, Motohashi H, Takayama O, Takae K, Nagai
699   Y, Seki K. 2017b. Generation of transgenic marmosets using a tetracyclin-inducible
700   transgene expression system as a neurodegenerative disease model. *Biology of*
701   *Reproduction* **97**:772–780. doi:10.1093/biolre/iox129

702 Van Essen DC, Smith SM, Barch DM, Behrens TEJ, Yacoub E, Ugurbil K. 2013. The WU-Minn
703   Human   Connectome   Project: An   overview.   *NeuroImage*   **80**:62–79.
704   doi:10.1016/j.neuroimage.2013.05.041

705 Vincent JL, Patel GH, Fox MD, Snyder AZ, Baker JT, Van Essen DC, Zempel JM, Snyder LH,
706   Corbetta M, Raichle ME. 2007. Intrinsic functional architecture in the anaesthetized
707   monkey brain. *Nature* **447**:83–86. doi:10.1038/nature05758

708   Wallis G, Stokes M, Cousijn H, Woolrich M, Nobre AC. 2015. Frontoparietal and Cingulo-

709   opercular Networks Play Dissociable Roles in Control of Working Memory. *Journal of*

710   *Cognitive Neuroscience* **27**:2019–2034. doi:10.1162/jocn_a_00838

711   Xiao Y, Beriault S, Pike GB, Collins DL. 2012. Multicontrast multiecho FLASH MRI for targeting

712   the subthalamic nucleus. *Magnetic Resonance Imaging* **30**:627–640.

713   doi:10.1016/j.mri.2012.02.006

714   Xiao Y, Fonov V, Bériault S, Subaie FA, Chakravarty MM, Sadikot AF, Pike GB, Collins DL. 2015.

715   Multi-contrast unbiased MRI atlas of a Parkinson's disease population. *International*

716   *Journal of Computer Assisted Radiology and Surgery* **10**:329–341. doi:10.1007/s11548-

717   014-1068-y

718   Yu H-H, Rosa MGP. 2010. A simple method for creating wide-field visual stimulus for

719   electrophysiology: Mapping and analyzing receptive fields using a hemispheric display.

720   *Journal of Vision* **10**:15. doi:10.1167/10.14.15

721   Zeater N, Buzás P, Dreher B, Grünert U, Martin PR. 2019. Projections of three subcortical visual

722   centers to marmoset lateral geniculate nucleus. *Journal of Comparative Neurology*

723   **527**:535–545. doi:10.1002/cne.24390

724